

# Supplemental material for “Single Laser Pulse Driven Thermal Limit of the Quasi-Two Dimensional Magnetic Ordering in Sr<sub>2</sub>IrO<sub>4</sub>”

R. Wang<sup>1,2,3</sup>, J. Sun<sup>1</sup>, D. Meyers<sup>4,5</sup>, J. Q. Lin<sup>1,2,3</sup>, J. Yang<sup>6</sup>, G. Li<sup>1</sup>, H. Ding<sup>2,3</sup>, Anthony D. DiChiara<sup>7</sup>, Y. Cao<sup>8</sup>, J. Liu<sup>6</sup>, M. P. M. Dean<sup>4</sup>, H. Wen<sup>7</sup>, and X. Liu<sup>1\*</sup>  
<sup>1</sup> School of Physical Science and Technology, ShanghaiTech University, Shanghai 201210, China.

<sup>2</sup> Beijing National Laboratory for Condensed Matter Physics and Institute of Physics, Chinese Academy of Sciences, Beijing 100190, China

<sup>3</sup> University of Chinese Academy of Sciences, Beijing 100049, China

<sup>4</sup> Condensed Matter Physics and Materials Science Department, Brookhaven National Laboratory, Upton, New York 11973, USA.

<sup>5</sup> Department of Physics, Oklahoma State University, Stillwater, Oklahoma 74078, USA.

<sup>6</sup> Department of Physics and Astronomy, University of Tennessee, Knoxville, Tennessee 37996, USA.

<sup>7</sup> Advanced Photon Source, Argonne National Laboratory, Argonne, IL, 60439, USA. and

<sup>8</sup> Materials Science Division, Argonne National Laboratory, Argonne, Illinois, 60439, USA.

## I. SAMPLE SYNTHESIS AND CHARACTERIZATION

Sr<sub>2</sub>IrO<sub>4</sub> thin film samples with thickness of  $\sim 100$  nm grown with PLD method were used[1]. Sr<sub>2</sub>IrO<sub>4</sub> is crystallized in  $I4_1/acd$  structure with single IrO<sub>2</sub> layers separated by SrO layers[2]. Each structural unit cell contains two Ir in one layer and four IrO<sub>2</sub> layers along c direction. The antiferromagnetic(AFM) ordering sets in at  $T_N \approx 240K$  for bulk crystal. In our thin film samples, the magnetic susceptibility measurement gave slightly lower  $T_N$  as shown in **Fig. S1**. The AFM ordering shares the same unit cell at that of the structure[3]. In the tetragonal Sr<sub>2</sub>IrO<sub>4</sub>, two twined magnetic domains are expected to produce two sets of magnetic reflection peaks at  $(1\ 0\ 4n)$ ,  $(0\ 1\ 4n+2)$  and  $(1\ 0\ 4n+2)$ ,  $(0\ 1\ 4n)$  respectively, where lattice reflections are forbidden. The magnetic ordering peaks from both domains were observed in the long range L-scan shown in **Fig. S2**, which are at  $(1\ 0$

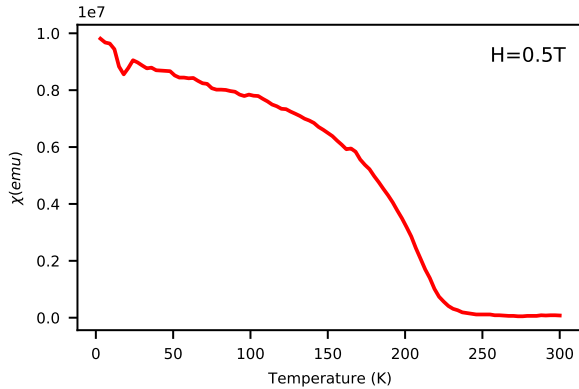


Fig. S 1: Temperature dependence of the magnetic susceptibility of our Sr<sub>2</sub>IrO<sub>4</sub> thin film sample.

\* liuxr@shanghaitech.edu.cn

16) and  $(1\ 0\ 18)$  respectively. Importantly, both peaks respond to laser stimulation in the same way.

## II. CHARACTERIZATION OF LASER SPOT AND ESTIMATION OF THE EFFECTIVE AVERAGE FLUENCE

Discrete laser pulses with a duration of  $\sim 100$  fs was used to pump the sample. The pump laser photon energy was selected to be 1 eV derived from a Ti: Sapphire laser system with an optical parametric amplifier, corresponding to the resonant excitation from  $J_{eff} = \frac{3}{2}$  to unoccupied  $J_{eff} = \frac{1}{2}$  states [4]. Thus the pumping largely creates double occupancy of the  $J_{eff} = \frac{1}{2}$  states and leaves a hole in the  $J_{eff} = \frac{3}{2}$  manifold. We have shown that 1eV pumping can efficiently break the long range AFM ordering[5]. The laser system runs at 1 KHz and can be controlled to deliver a single-shot laser pulse on demand.

To properly characterize the laser fluence, the laser power density profile was measured, as shown in **Fig. S3**. The profile can be modeled as an isotropic Gaussian pulse with the fitted  $\sigma$  to be  $350\mu\text{m}$ . In the experiment, the laser incident angle was  $47^\circ$ . Thus the laser on-sample footprint was elongated along one direction with  $\sigma' = \sigma/\sin(47^\circ) = 479\mu\text{m}$ . The effective laser fluence under the X-ray spot can be calculated as,

$$F = \frac{P}{Af} \iint_A \frac{1}{2\pi\sigma\sigma'} \exp[-(\frac{x^2}{\sigma^2} + \frac{y^2}{\sigma'^2})] dx dy \quad (1)$$

where A is the overlapped area of the X-ray at the laser spot center on the sample surface,  $f$  is the running frequency as 1 kHz, and  $P$  is the laser power measured during the experiments. At  $P = 1mW$  with  $A = 2.41 \times 10^{-4}cm^2$ , the average fluence within the overlapped region of the single laser shot and X-ray beam spot on the sample is  $0.113\ mJ/cm^2$ . As the X-ray to the laser spot center overlap was done by referring to a video camera monitor, we expect certain miss-alignment.

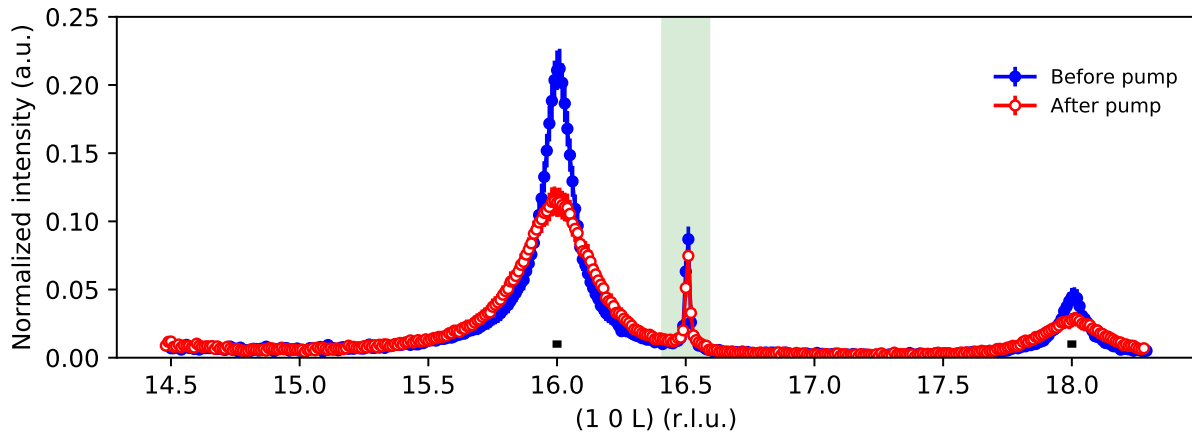


Fig. S 2: Long-range L-scan of (1 0 L) magnetic Bragg peaks along c-axis direction. The long-range reciprocal space scan along out-of-plane direction(L scan) was performed for pristine thermal equilibrium condition of the sample at 80K(blue) and after the first single laser shot(red). The appearance of both (1 0 16) and (1 0 18) magnetic Bragg peaks indicate the existence of twinned magnetic domains $[(1 0 4n),(0 1 4n+2)]$  and  $[(1 0 4n+2),(0 1 4n)]$  in our sample. Both of these two magnetic domains respond to the single shot in a similar manner. The horizontal small bars represents the instrumental resolution. The peak at  $L = 16.5$ (marked by the shaded region) comes from the  $(\frac{1}{2} \frac{5}{2})$  superlattice peak of the SrTiO<sub>3</sub> substrate.

In **Fig. 3** in the main text, the error bar given for fluence is 10% by assuming possible  $\pm 60\mu\text{m}$  miss-alignment.

At  $\sim 1\text{eV}$ , the penetration depth of the pumping laser for Sr<sub>2</sub>IrO<sub>4</sub> is estimated[5] to be  $\sim 100\text{ nm}$ .

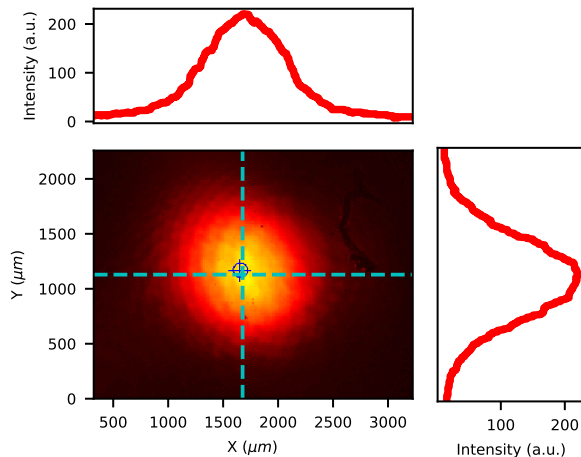


Fig. S 3: Characterization of the laser spot size. The energy density profile of the pump laser was measured with CCD, as shown in the image. Two line cuts (shown by the dashed lines in the CCD image) were taken to extract the peak widths. From Gaussian fitting, both directions give  $\sigma = 350\mu\text{m}$ .

### III. SCHEMATIC OF EXPERIMENT

The X-ray resonant magnetic scattering(XRMS) measurements were conducted at the Advanced Photon Sources(APS) using beamline 7-ID-C. The data were collected at Ir  $L_3$  absorption edge of 11.216 KeV. A horizontal scattering geometry was used.(see **Fig. S4**) The laser pulse came in at a large angle of  $47^\circ$  relative to the sample surface to allow a more homogeneous excitation along the sample depth direction.

To amplify the magnetic scattering signal[6], the scattering experiment was performed in the  $a$ - $c$  plane with the incident X-ray came in at a shallow angle of  $4.87^\circ$  relative to the sample surface. Its polarization was almost parallel to the sample surface  $c$ -direction. A Pilatus CCD with pixel size of  $172\mu\text{m}^2$  was used in the experiment to monitor the scattered X-ray signal. It was placed  $\sim 1\text{m}$  away from the sample, which gives an angular resolution of  $0.01^\circ$  per pixel. The sample was cooled down to 80 K with cryostat, well below the Néel ordering temperature. During the experiment, a full thermal cycle was done by warming the sample up to 280 K and then slowly cooling down to 80 K with a cooling rate of 0.05 K/s. The laser induced suppression of the magnetic peak height was fully recovered after a thermal cycle, as shown in the cross-sample scan in **Fig. S5**. The entire process is repeatable, ruling out the irreversible sample damage issue.

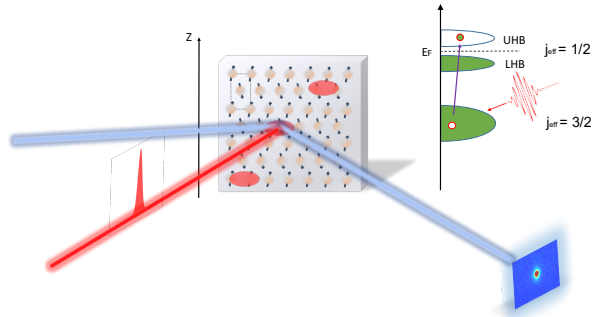


Fig. S 4: Experimental configuration. The XRMS experiment was performed in a horizontal scattering geometry where the  $a$ - and  $c$ -axis of sample lie within the scattering plane. Three far-apart separated spots on the sample were chosen to be measured in between slow thermal-cycle processes to save experimental time. The inset shows the corresponding electron excitations from laser pumping, where 1 eV laser pulses mainly drive electrons from  $J_{eff} = \frac{3}{2}$  states into the unoccupied  $J_{eff} = \frac{1}{2}$  states.

#### IV. LASER EFFECT ON STRUCTURAL PEAK

To check the laser shot effect on the crystal structure,  $(0\ 0\ 16)$  structure peak height was monitored with single laser pulse stimulation. As shown in **Fig. S6**, the fluctuation in the structural peak height, mainly due to X-ray beam instability, is uncorrelated with the laser stimulation. Thus laser induces minimum effect to the lattice at 1Hz frequency of which our data was taken, and the suppression of the magnetic peak height is intrinsic to the spin sector.

#### V. X-RAY EFFECT ON MAGNETIC PEAK

We checked the X-ray effect on magnetic peak by monitoring the  $(1\ 0\ 16)$  magnetic Bragg peak height after X-ray was initially turned on after a full thermal cycle, without any optical pumping on sample. A gradual reduction of the peak height about 7% was noticed after the X-ray exposure of the sample, as shown in **Fig. S7**. Then the peak height stabilized after a few minutes.

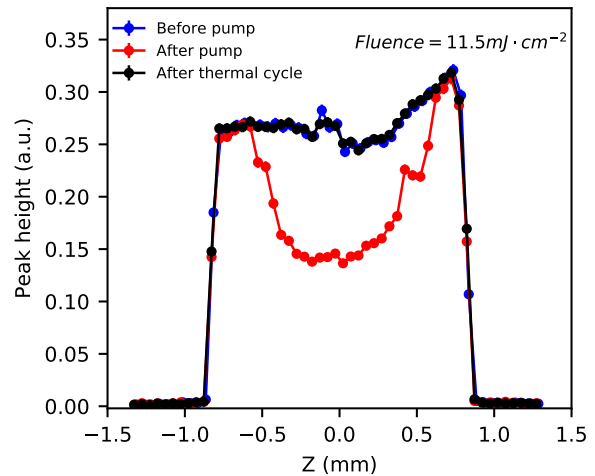


Fig. S 5: Cross-sample scan. Real space scans along  $z$ -direction (see the experimental schematic in **Fig. S4**) across the sample while monitoring the  $(1\ 0\ 16)$  magnetic peak height. Three scans were taken for: pristine thermal equilibrium condition (blue curve), after single laser pulse excitation (red curve), and after a full thermal cycle process (black curve). The laser pumping leads to a drastic suppression of the scattering intensity, which is fully recovered after a thermal cycle.

#### VI. FORMULA FOR THE DIFFRACTION PROFILE OF THE L-SCAN OF MAGNETIC BRAGG PEAK

Since the in-plane AFM ordering correlation length is fully restored, we focus on the inter-plane correlation. A phenomenological model is constructed by assuming

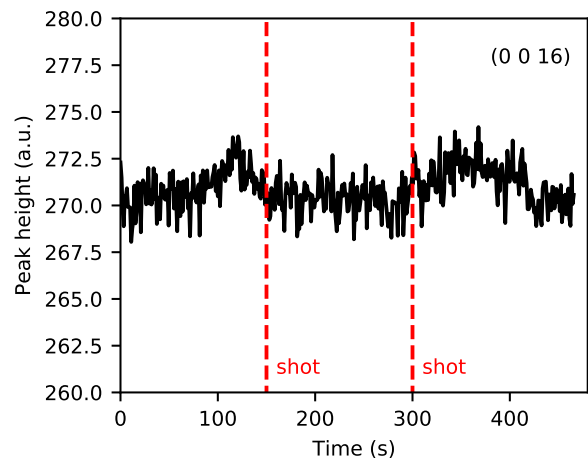


Fig. S 6: Laser effect on structural peak. response of the  $(0\ 0\ 16)$  structural Bragg peak height to laser stimulation. The dashed lines mark two single laser pulses.

the AFM ordered iso-spins are still pointing to the crystal  $a$ -direction as in the thermal equilibrium state while their inter-plane correlation is described by an exponential decay as  $e^{-\frac{|z_m - z_n|}{\xi}}$  with  $z_{m(n)}$  to be the  $c$ -direction

coordinate. Accordingly, the magnetic reflection intensity can be written as,

$$I(Q_z, \xi_z) = |F|^2 \left[ \delta(Q_x - h \cdot a^*) \delta(Q_y - k \cdot b^*) \right]^2 \cdot \frac{1}{N_3} \sum_{j,k=1}^{N_3} (-1)^j e^{-iQ_z z_j} (-1)^k e^{iQ_z z_k} e^{-\frac{|z_j - z_k|}{\xi_z}} \quad (2)$$

where  $F$  is the magnetic scattering factor for Ir sites, and  $j$  and  $k$  represents the  $j$ -th and  $k$ -th plane along  $c$ -direction.  $N_3$  is the total plane number along  $c$ -direction.  $\xi_z$  is the  $c$ -direction magnetic correlation length. The in-plane structure factors are simplified to  $\delta$ -functions due to the fact that the in-plane correlation lengths are orders of magnitude larger than the  $c$ -direction correlation length(see main text). The summation can be analytically carried out as:

$$I(Q_z, \xi_z) = |F|^2 \frac{\sinh(\frac{d}{\xi_z})}{\cosh(\frac{d}{\xi_z}) - \cos(Q_z d)} \quad (3)$$

where  $d$  is the inter-layer distance.

The relative momentum transfer can be defined as  $q_z = Q_z - G$  with  $G$  indexing the Bragg points. When  $\frac{(q_z d)^4}{4!} \ll 1$ , close to the Bragg point as where our  $L$ -scans were taken, Eqn. 3 can be simplified as:

$$I(q_z, \xi_z) = |F|^2 \frac{\sinh(\frac{d}{\xi_z})}{\cosh(\frac{d}{\xi_z}) - \cos(q_z d)} \quad (4)$$

$$\approx |F|^2 \frac{(\frac{d}{\xi_z})}{\frac{d^2}{2\xi_z^2} + \frac{(q_z)^2}{2}} \quad (5)$$

$$= |F|^2 \frac{2}{d} \frac{\xi_z}{1 + q_z^2 \xi_z^2} \quad (6)$$

Thus, with inter-layer ordering correlation defined as  $e^{-\frac{|z_m - z_n|}{\xi_z}}$ , the X-ray scattering profile is of a Lorentzian shape. The peak height at  $q_z = 0$  should be proportional to the correlation length  $\xi_z$ , while the whole integrated intensity is constant. All these predictions agree well with our observations, suggesting a quite homogeneous statistical distribution of the  $c$ -direction spin ordering.

## VII. FITTING PROCEDURE OF THE MAGNETIC BRAGG PEAK

All the magnetic peaks were fitted based on the Eqn. 6 plus a linear background intensity, as shown in Eqn. 7. For a set of magnetic Bragg peaks studied with the same fluence of laser pulse, firstly we fit the magnetic Bragg peaks of pristine thermal limit(before laser excitation), and extract a background intensity; Then we fit the magnetic Bragg peaks after the single shot excitation with the same background intensity.(see **Fig. S8b**)

$$I(q_z, h, \xi_z) = \frac{2}{d} \frac{h}{1 + q_z^2 \xi_z^2} + I_{bg} \quad (7)$$

The fitting was done by least-squares fitting. And here the reduced Chi-square  $\chi_\nu^2$  is defined as:

$$\chi_\nu^2 = \frac{1}{N - N_{varys}} \sum_i^N \frac{[y_i^{exp} - y_i^{model}(v)]^2}{\epsilon_i^2} \quad (8)$$

where  $N$  is the number of data points,  $N_{varys}$  is the number of variables in the fit,  $y_i^{exp}$  is the measured data,  $y_i^{model}(v)$  is the model calculation and  $v$  is the set of variables in the model to be optimized in the fit, and  $\epsilon_i$  is the estimated uncertainty in the data.

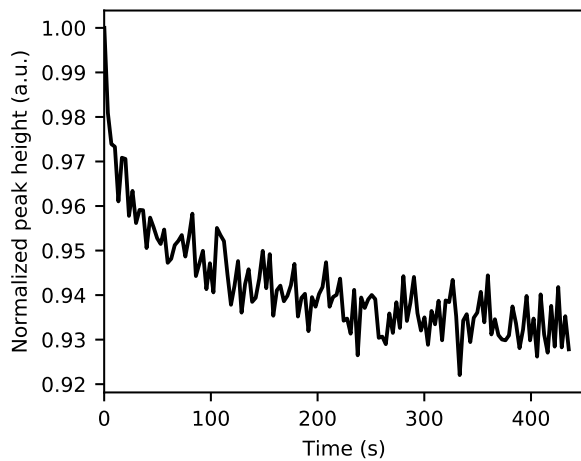


Fig.S 7: X-ray effect on magnetic peak. Temporal evolution of the (1 0 16) magnetic Bragg peak height (normalized) in the initial 420 seconds after turning on the X-ray.

TABLE I: Fitting goodness

Fluence( $mJ/cm^2$ )	1.0	3.3	6.0	6.8	9.4	11.9	13.1	18.5
$\chi^2_\nu$	18.4	21.6	30.7	8.5	4.9	8.7	6.8	6.2

Representative fitting goodness is listed in Table. SI. And we plot three of the typical fitting results in **Fig. S8a**.

### VIII. MULTIPLE SHOTS EVOLUTION OF THE MAGNETIC PEAK HEIGHT

Magnetic peak height was measured upon a sequence of laser shots of various fluences. As shown in **Fig. S9**, each of the first a few shots induced certain degree of suppression to the magnetic peak height. After those initial shots, the peak height does fully recover, but only to a reduced level prepared by the initial multiple pulses. The stabilized conditions are obviously dependent on the laser pulse fluence.

### IX. MODELING THE THICKNESS DEPENDENCE OF THE AFM ORDERING AT FINITE TEMPERATURE

We evaluate the saturation of the low limit of the observed inter-plane correlation by considering a minimum Quasi-2D spin model. As shown in **Fig. S10**, spin-1/2 objects are placed at the Ir sites which are AFM ordered, forming spin-up (A) and spin-down (B) sublattices. The exchange interactions considered are: the nearest-neighbor in-plane AFM exchange  $J$ , the inter-plane next-nearest-neighbor exchange  $J_{1c}$  and  $J_{2c}$  for the coupling within and between the spin-up and spin-down sublattices. Also, the anisotropy of the nearest-neighbor exchange,  $\Delta$ , is considered. As a result, the Hamiltonian for this minimum spin model can be written as[7, 8],

$$\begin{aligned}
H &= \frac{J}{2} \sum_{l<ij>} \vec{S}_l \cdot \vec{S}_j + \Delta \sum_{l<ij>} S_{li}^z S_{lj}^z + \frac{J_c}{2} \sum_{\langle ll' \rangle \langle ij \rangle} \vec{S}_l \cdot \vec{S}_{l'} \\
&= \frac{J}{2} [D \sum_{l<ij>} S_{lAi}^z S_{lBj}^z + \frac{1}{2} \sum_{l<ij>} (S_{lAi}^+ S_{lBj}^- + S_{lAi}^- S_{lBj}^+)] \\
&\quad + J [D \sum_{l<ij>} S_{lBi}^z S_{lAj}^z + \frac{1}{2} \sum_{l<ij>} (S_{lBi}^+ S_{lAj}^- + S_{lBi}^- S_{lAj}^+)] \\
&\quad + \frac{J_{1c}}{2} [ \sum_{\langle ll' \rangle} \sum_{\langle ij \rangle} S_{lAi}^z S_{l' Aj}^z + \frac{1}{2} \sum_{\langle ll' \rangle} \sum_{\langle ij \rangle} (S_{lAi}^+ S_{l' Aj}^- + S_{lAi}^- S_{l' Aj}^+)] \\
&\quad + \frac{J_{1c}}{2} [ \sum_{\langle ll' \rangle} \sum_{\langle ij \rangle} S_{lBi}^z S_{l' Bj}^z + \frac{1}{2} \sum_{\langle ll' \rangle} \sum_{\langle ij \rangle} (S_{lBi}^+ S_{l' Bj}^- + S_{lBi}^- S_{l' Bj}^+)] \\
&\quad + \frac{J_{2c}}{2} [ \sum_{\langle ll' \rangle} \sum_{\langle ij \rangle} S_{lAi}^z S_{l' Bj}^z + \frac{1}{2} \sum_{\langle ll' \rangle} \sum_{\langle ij \rangle} (S_{lAi}^+ S_{l' Bj}^- + S_{lAi}^- S_{l' Bj}^+)] \\
&\quad + \frac{J_{2c}}{2} [ \sum_{\langle ll' \rangle} \sum_{\langle ij \rangle} S_{lBi}^z S_{l' Aj}^z + \frac{1}{2} \sum_{\langle ll' \rangle} \sum_{\langle ij \rangle} (S_{lBi}^+ S_{l' Aj}^- + S_{lBi}^- S_{l' Aj}^+)]
\end{aligned} \tag{9}$$

where  $D$  is defined as  $D = 1 + \Delta$ .

To compare with our experimental observations on  $\text{Sr}_2\text{IrO}_4$ , we refer to the published literature[9–11] and set,

- Nearest neighbor exchange interaction  $J = 60 \text{ meV}$
- Interlayer exchange interaction: within the same sublattice  $J_{1c} = -16.4 \text{ } \mu\text{eV}$ ; between the two sublattices  $J_{2c} = 16.4 \text{ } \mu\text{eV}$

- the anisotropic term related to the magnon gap as  $E(k) = ZJ\langle Sz \rangle \sqrt{D^2 - \gamma_k^2}$

As the reported exchange anisotropy for  $\text{Sr}_2\text{IrO}_4$  is quite controversial[9–13], the gap size was carried as a free parameter in our calculation. The dynamics of the above Hamiltonian was solved with the equation of motion technique and mean-field approximation for model systems with different thickness.

Using the equation of motion of double-time Green's function[7, 8, 14], we can obtain a set of Green's functions for each layer:

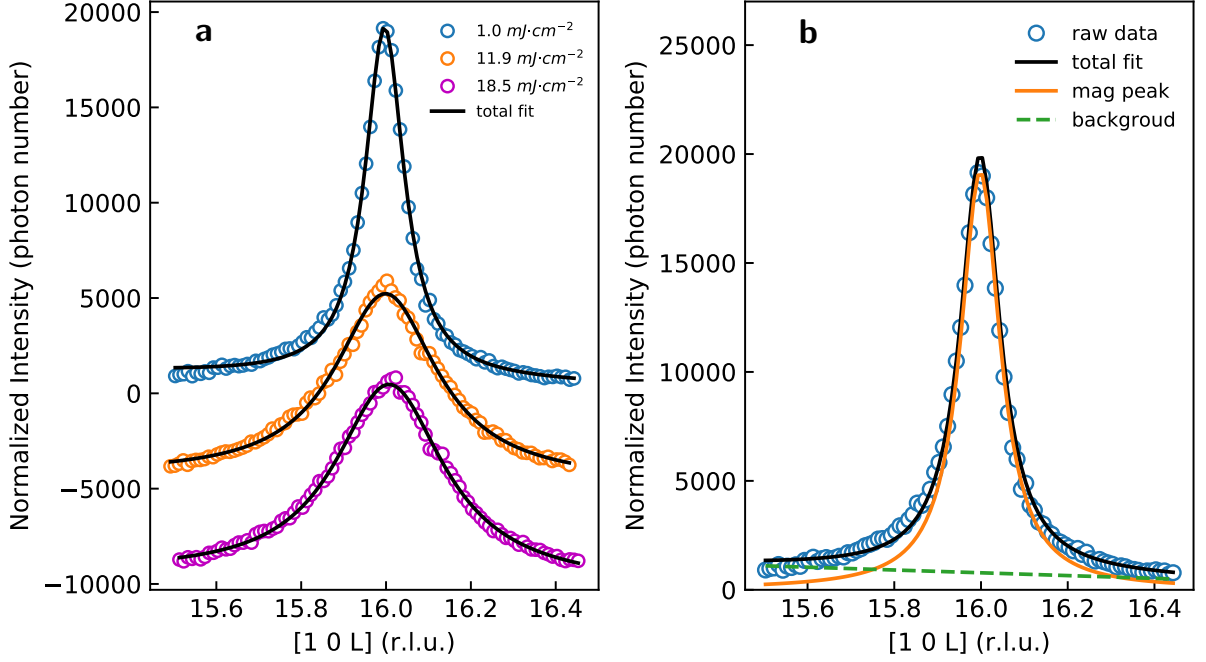


Fig. S 8: **Fitting Procedure of Magnetic Bragg Peak:** All the magnetic Bragg peaks were fitted with the Lorentzian function we derived with a linear background (Eqn. 7) using the least-squares fitting method. **a**, Three L-scan data after laser excitation and the fitting results (vertically stacked for clarity). **b**, The fitting components of a typical L-scan data.

$$\begin{aligned}
& [\omega - JDZ\langle S_l^z \rangle + Z'(J_{1c} - J_{2c})(\langle S_{l+1}^z \rangle + \langle S_{l-1}^z \rangle)]g_{ll} - J\langle S_l^z \rangle Z\gamma(k)f_{ll} \\
& - J_{1c}Z'\gamma_{AA}(k)(g_{l-1,l}(k) + g_{l+1,l}(k)) - J_{2c}Z'\gamma_{AB}(k)(f_{l-1,l}(k) + f_{l+1,l}(k)) = 2\langle S_l^z \rangle \\
& [\omega + JDZ\langle S_l^z \rangle - Z'(J_{1c} - J_{2c})(\langle S_{l+1}^z \rangle + \langle S_{l-1}^z \rangle)]f_{ll} + J\langle S_l^z \rangle Z\gamma(k)g_{ll} \\
& + J_{1c}Z'\gamma_{AA}(k)(f_{l-1,l}(k) + f_{l+1,l}(k)) + J_{2c}Z'\gamma_{AB}(k)(g_{l-1,l}(k) + g_{l+1,l}(k)) = 0 \\
& [\omega - JDZ\langle S_{l-1}^z \rangle + Z'(J_{1c} - J_{2c})(\langle S_l^z \rangle + \langle S_{l-2}^z \rangle)]g_{l-1,l} - J\langle S_{l-1}^z \rangle Z\gamma(k)f_{l-1,l} \\
& - J_{1c}Z'\gamma_{AA}(k)\langle S_{l-1}^z \rangle(g_{l-2,l}(k) + g_{l,l}(k)) - J_{2c}Z'\gamma_{AB}(k)\langle S_{l-1}^z \rangle(f_{l-2,l}(k) + f_{l,l}(k)) = 0 \\
& [\omega + JDZ\langle S_{l-1}^z \rangle - Z'(J_{1c} - J_{2c})(\langle S_{l-2}^z \rangle + \langle S_l^z \rangle)]f_{l-1,l} + J\langle S_{l-1}^z \rangle Z\gamma(k)g_{l-1,l} \\
& + J_{1c}Z'\gamma_{AA}(k)\langle S_{l-1}^z \rangle(f_{l-2,l}(k) + f_{l,l}(k)) + J_{2c}Z'\gamma_{AB}(k)\langle S_{l-1}^z \rangle(g_{l,l-2}(k) + g_{l,l}(k)) = 0
\end{aligned} \tag{10}$$

Where  $N$  is the total number of layers, and  $l$  is the index of each layer ( $l = 1, 2, \dots, N$ ).  $Z, Z'$  are the in-plane and out of plane coordinate numbers.  $g_{ll}(k)$  and  $f_{ll}(k)$  are Fourier transformation of  $G_{ll}(\omega)$  and  $F_{ll}(\omega)$  in  $k$ -space.  $\gamma$ 's are the geometry factors:

- $\gamma(k)$ : in-plane between A and B Ir atoms
- $\gamma_{AA}(k)$ : Nearest layers between A-A or B-B Ir atoms
- $\gamma_{AB}(k)$ : Nearest layers between A-B Ir atoms

The equation of motion was solved self-consistently for  $T = 80$  K, which is our experimental temperature. Once the local correlation function,

$$\langle S_l^- S_l^+ \rangle = \frac{i}{2\pi} \int_{-\infty}^{\infty} \frac{d\omega}{e^{\frac{\omega}{k_B T}} + 1} \{g_{ll}(\omega + i0^+) - g_{ll}(\omega - i0^-)\} \tag{11}$$

is obtained from the closed self-consistent loop, the local magnetic moments  $\langle S_l^z \rangle$  of each layer,

$$\langle S_l^z \rangle = \frac{1}{2} - \langle S_l^- S_l^+ \rangle \tag{12}$$

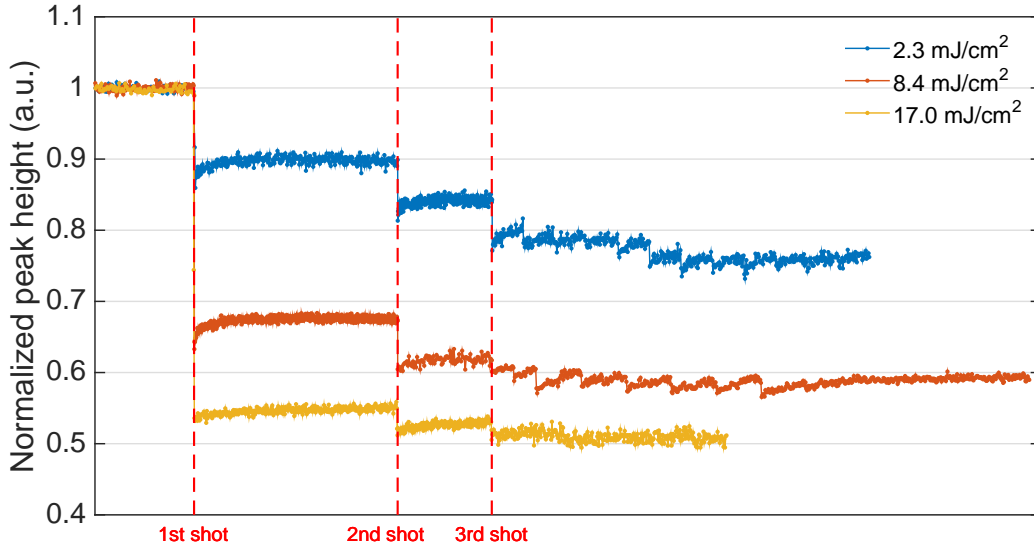


Fig. S 9: **Evolution of the magnetic peak height under excitation of multiple shots:** The pristine magnetic order was degraded by a sequence of single laser shots, the first three single shots were marked by red dashed lines. With increasing the laser fluence, the degree of the suppression of magnetic order keep reducing in the first initial stage where permanent suppression occurs; At high fluence, the multiple shots after the very first single shot drives marginal further suppression to the magnetic order and the system enters into a stable stage.

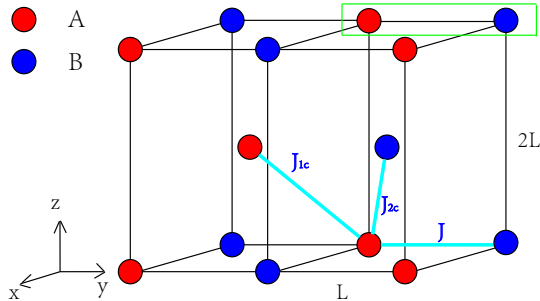


Fig. S 10: **Minimum model of an AFM ordered spin-1/2 system:** The ordered spins are grouped into the spin-up (A) and spin-down (B) sub-lattices. The exchange terms considered are labeled accordingly.

was extracted and plotted as **Fig. 4** in the main text.

- 
- [1] C. Rayan Serrao, J. Liu, J. T. Heron, G. Singh-Bhalla, A. Yadav, S. J. Suresha, R. J. Paull, D. Yi, J. H. Chu, M. Trassin, et al., Epitaxy-Distorted Spin-Orbit Mott Insulator in  $\text{Sr}_2\text{IrO}_4$  Thin Films, *Phys. Rev. B* 87, 085121 (2013).
- [2] Q. Huang et al., Neutron Powder Diffraction Study of the Crystal Structures of  $\text{Sr}_2\text{RuO}_4$  and  $\text{Sr}_2\text{IrO}_4$  at Room Temperature and at 10 K, *J. Solid State Chem.* 112, 355 (1994).
- [3] S. Fujiyama, H. Ohsumi, T. Komesu, J. Matsuno, B. J. Kim, M. Takata, T. Arima, and H. Takagi, Two-Dimensional Heisenberg Behavior of  $J_{\text{eff}}=1/2$  Isospins in the Paramagnetic State of the Spin-Orbital Mott Insulator  $\text{Sr}_2\text{IrO}_4$ , *Phys. Rev. Lett.* 108, 247212 (2012).
- [4] S. J. Moon, H. Jin, W. S. Choi, J. S. Lee, S. S. A. Seo, J. Yu, G. Cao, T. W. Noh, and Y. S. Lee, Temperature Dependence of the Electronic Structure of the  $J_{\text{eff}}=1/2$  Mott Insulator  $\text{Sr}_2\text{IrO}_4$  Studied by Optical Spectroscopy, *Phys. Rev. B* 80, 195110 (2009).
- [5] M. Dean, Y. Cao, X. Liu, S. Wall, D. Zhu, R. Mankowsky, V. Thampy, X. M. Chen, J. G. Vale, D. Casa et al., Ultrafast Energy- and Momentum-Resolved Dynamics of Magnetic Correlations in the Photo-Doped Mott Insulator  $\text{Sr}_2\text{IrO}_4$ , *Nat. Mater.* 15, 601 (2016).

- [6] X. Liu, T. Berlijn, W.-G. Yin, W. Ku, A. Tsvelik, Y.-J. Kim, H. Gretarsson, Y. Singh, P. Gegenwart, and J. P. Hill, Long-Range Magnetic Ordering in  $\text{Na}_2\text{IrO}_3$ , *Phys. Rev. B* 83, 220403(R) (2011).
- [7] H. Diep, Quantum Effects in Heisenberg Antiferromagnetic Thin Films, *Phys. Rev. B* 43, 8509 (1991).
- [8] A. Moschel, and K. D. Usadel, Magnetization of Coupled Ferromagnetic and Antiferromagnetic Films: Dependence on the Interface Coupling, *Phys. Rev. B* 48, 13991 (1993).
- [9] J. Porras, J. Bertinshaw, H. Liu, G. Khaliullin, N. H. Sung, J.-W. Kim, S. Francoual, P. Steffens, G. Deng, M. M. Sala, A. Efimenko, A. Said, D. Casa, X. Huang, T. Gog, J. Kim, B. Keimer, and B. J. Kim, Pseudospin-Lattice Coupling in the Spin-Orbit Mott Insulator  $\text{Sr}_2\text{IrO}_4$ , *Phys. Rev. B* 99, 085125 (2019).
- [10] Y. Gim, A. Sethi, Q. Zhao, J. F. Mitchell, G. Cao, and S. L. Cooper, Isotropic and Anisotropic Regimes of the Field- Dependent Spin Dynamics in  $\text{Sr}_2\text{IrO}_4$ : Raman Scattering Studies, *Phys. Rev. B* 93, 024405 (2016).
- [11] S. Calder, D. M. Pajerowski, M. B. Stone, and A. F. May, Spin-Gap and Two-Dimensional Magnetic Excitations in  $\text{Sr}_2\text{IrO}_4$ , *Phys. Rev. B* 98, 220402(R) (2018).
- [12] D. Pincini, J. G. Vale, C. Donnerer, A. de la Torre, E. C. Hunter, R. Perry, M. Moretti Sala, F. Baumberger, and D. F. McMorrow, Anisotropic Exchange and Spin-Wave Damping in Pure and Electron-Doped  $\text{Sr}_2\text{IrO}_4$ , *Phys. Rev. B* 96, 075162 (2017).
- [13] S. Bahr, A. Alfonsov, G. Jackeli, G. Khaliullin, A. Matsumoto, T. Takayama, H. Takagi, B. Bchner, and V. Kataev, Low-Energy Magnetic Excitations in the Spin-Orbital Mott Insulator  $\text{Sr}_2\text{IrO}_4$ , *Phys. Rev. B* 89, 180401(R) (2014).
- [14] P. Fröbrich, and P. J. Kuntz, Many-Body Green's Function Theory of Heisenberg Films, *Phys. Rep.* 432, 223 (2006).